Geochemical Perspectives Letters

Past endolithic life in metamorphic ocean crust

X. Peng[1], Z. Guo[2,1*], M. Du[1], A.D. Czaja[3], D. Papineau[4], S. Chen[1], H. Xu[1], J. Li[1], K. Ta[1], S. Bai[1], S. Dasgupta[1]

OPEN ACCESS

doi: 10.7185/geochemlet.2017

Abstract

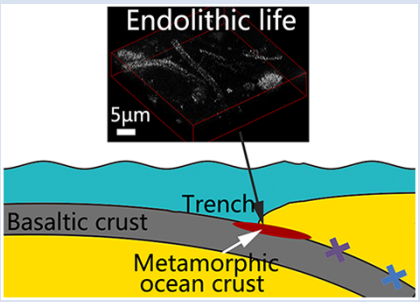

The known deep subsurface biosphere on Earth persists in diversified habitats, including deep within igneous rocks of the oceanic crust. Here, we extend the range of the deep subsurface biosphere to metamorphic ocean crust of a subduction zone. We report fossilised life in zeolite facies rocks, which formed by low grade metamorphism, from the southern Mariana trench. Dense carbonaceous spheroids, filaments, and *Frutexites*-like structures are preserved in these rocks, which are enriched in organic carbon but depleted in ^{13}C. The distinct difference in the GDGT-0 *vs.* crenarchaeol and the branched *vs.* isoprenoid tetraether values between the inner and outer portions of these rocks indicate the *in situ* production of organic carbon. We demonstrate that these structures may result from the past activity of potential chemolithoautotrophs within the metamorphic crust, as implied by their morphologies, Raman spectra, carbon isotopes, and biomarker signatures, as well as the Fe oxidation state within whole rocks. We propose that fluid-rock reactions at temperatures within the tolerance of life during low grade metamorphism contributed to microbial subsistence within the biotope. The low grade metamorphic ocean crust of the subduction zone likely represents Earth's deepest, and one of its largest, microbial ecosystems, which may potentially influence the deep carbon cycle.

Received 21 July 2019 | Accepted 28 April 2020 | Published 26 June 2020

Letter

The deep subsurface biosphere on Earth exists in a variety of hydrated subsurface regions with sufficient energy gradients (Orsi, 2018). Furnes *et al.* (2008) reviewed the microbial alteration textures in the meta-volcanic glasses and crusts of pillow lavas from submarine environments, showing that textural signatures and chemical tracers of microbial life can be well preserved in metamorphic rocks. Based on a heat conduction model, Plümper *et al.* (2017) estimated that microbial life could exist as deep as ~10 km below the seafloor. However, little is known about whether microbial life thrives in metamorphic rocks that form under low temperature, high pressure conditions at a convergent margin during the descent of a subducting plate. Among these metamorphic rocks, zeolite facies rocks (Fig. S-1) are first formed from metamorphism of basaltic rocks in subduction zones at depths of 1–14 km beneath the seafloor and temperatures of approximately 40–300 °C (Marshak, 2009). The temperature range of zeolite facies formation is partly within the tolerance of life (Takai *et al.*, 2008), making it the maximum metamorphic grade that can potentially host life in subduction zones. Thus, zeolite facies rocks in subduction zones may provide promising habitats for subsurface piezophilic microorganisms.

To test this hypothesis, we recovered metamorphic rocks that have been tectonically extruded through deep faults at the seafloor from the subduction zone of the southern Mariana trench (SMT) at a water depth of 5500 to 6800 m (Fig. S-2, Table S-1), using the manned submersible *Jiaolong* during two R/V *XYH09* cruises (June–July 2016 and May–June 2017). Extensive outcrops of metamorphic rocks were observed on the south and north slopes of the SMT (Fig. 1). X-ray diffraction (XRD) analyses show that these metamorphic rocks mainly consist of phillipsite, heulandite, gmelinite, analcite, natrolite, chabasite, chlorite, and celadonite (Table S-1), a mineral assemblage indicative of low grade zeolite facies metamorphism. The oxygen isotopic composition of carbonates extracted from these rocks ($\delta^{18}O_{SMOW}$ = 13.9 to 25.3 ‰) reveals that they have been altered at temperatures between 20 °C and 89 °C assuming equilibrium with ^{18}O-depleted fluids (–4 ‰; Table S-2).

Transmitted white light and scanning electron microscopy (SEM) observations revealed a high abundance of spheroidal objects with diameters of *ca.* 2–150 μm in zeolite and celadonite (Figs. 2a,b, S-3, S-4). They exhibit loose, net-like, or condensed-gel structures (Fig. S-4d). Nano-scale secondary ion mass spectrometry (NanoSIMS) and energy dispersive X-ray spectroscopy (EDS) element maps show that the spheroids are chiefly composed of carbon (C), nitrogen (N) and phosphorus (P), whereas the matrix is zeolite or celadonite (Figs. 2d–g, S-3c,f, S-4e, S-5). Raman spectra of the carbonaceous spheroids are characterised by two broad and overlapped first order bands, assigned as

1. Institute of Deep Sea Science and Engineering, Chinese Academy of Sciences, Sanya 572000, China
2. College of Resource and Environmental Sciences, Hebei Normal University, Shijiazhuang 050024, China
3. Department of Geology, University of Cincinnati, Cincinnati, OH 45221, USA
4. Department of Earth Sciences, London Centre for Nanotechnology, and Centre for Planetary Science, University College London, 17-19 Gordon Street, London, WC1H 0AH, United Kingdom

* Corresponding author (email: guozx@idsse.ac.cn)

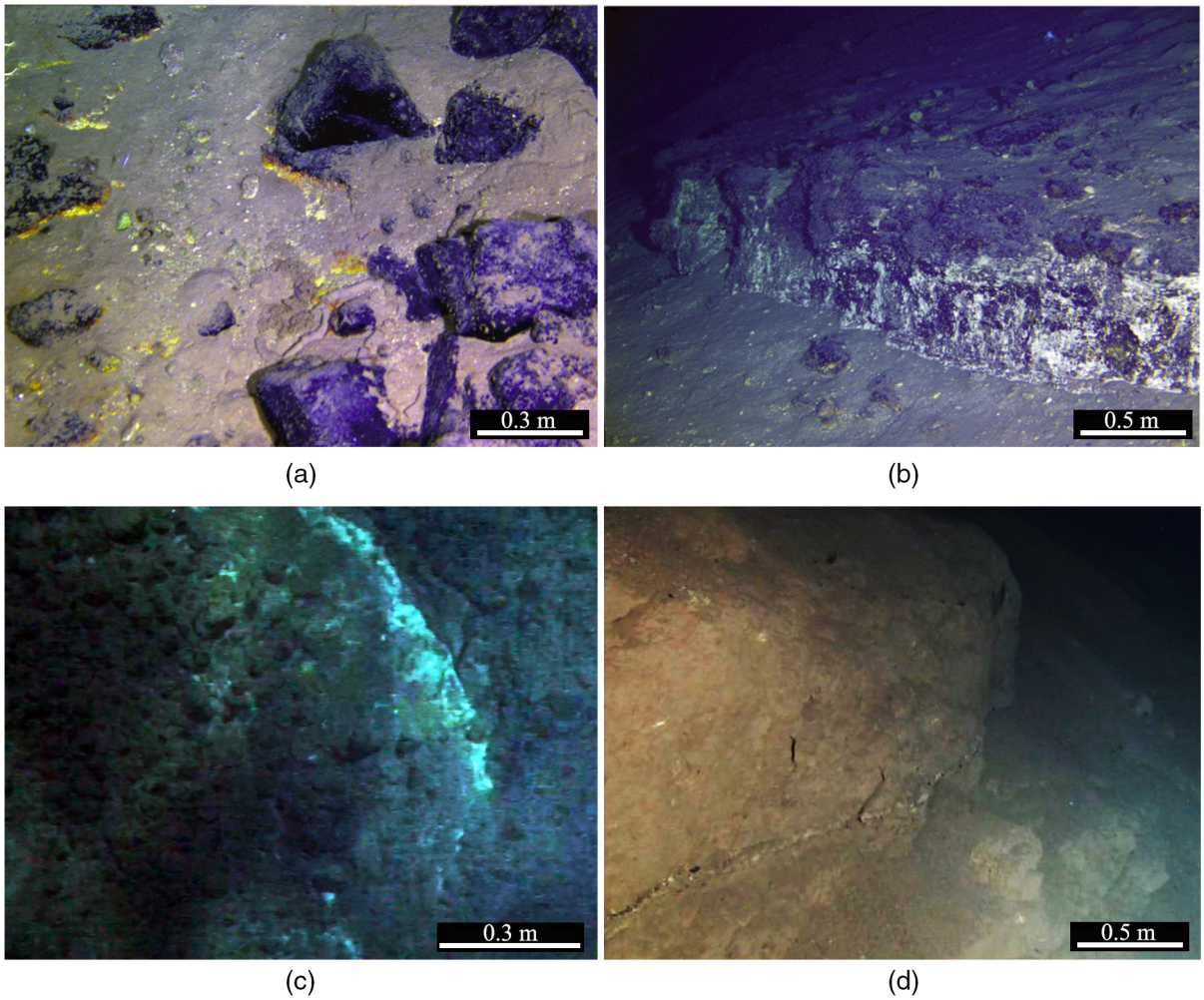

Figure 1 Representative metamorphic ocean crust on the north **(a-b)** and south **(c-d)** slopes of the SMT. **(a)** Yellow-green zeolite rocks coated by black manganese crusts (Dive JL118; 6695 mbsl). **(b)** White-yellow zeolite rock terrace (Dive JL119; 6001 mbsl). **(c)** Bluish-green celadonite rock outcrop (Dive JL122; 6300 mbsl). **(d)** Yellowish zeolite mound (Dive JL122; 6296 mbsl). Zeolite rocks in yellow indicate the presence of ferric iron.

D and G, and a very wide second order band of disordered carbonaceous matter (DCM; Fig. 2c). The morphologies and chemical compositions of the SMT carbonaceous spheroids resemble those of a fossilised microbial community found in serpentinised mantle rocks (Klein *et al.*, 2015; Plümper *et al.*, 2017).

Microscopic filaments, which are composed of DCM (Figs. 2i,j, S-6b; Video S-1), are also present in the SMT metamorphic rocks (Figs. 2h, S-6a,c,d). These filaments, ~2.0 μm wide and ~30–200 μm long, are typically tubular, non-septate and unbranched. The tubular nature of the carbonaceous filaments, the existence of a "hollow" lumina shown in Video S-1, and the range of widths exhibited by the filaments, are consistent with a biological origin (Buick, 1990). Morphologically, they resemble microbial filaments found in zeolite-carbonate interfaces in subseafloor basalts (Ivarsson *et al.*, 2008).

Millimetre scale *Frutexites*-like structures composed of zeolite and celadonite also occur in the matrix (Figs. 2k,l, S-7; see Supplementary Information). The close spatial associations and bulbous arborescent morphology of the SMT *Frutexites*-like structures, as well as the occurrence of carbonaceous matter concentrated in zeolite and celadonite minerals, indicate that the organic matter may have been formed by microbial activity during subduction metamorphism. Similar *Frutexites*-like structures were previously found in subsurface rock samples and attributed to chemoautotrophic communities (Heim *et al.*, 2017).

Geochemical analyses show that contents of total organic carbon (TOC) in metamorphic rocks range from 0.008 wt. % to 0.379 wt. %, while contents of total inorganic carbon (TIC) range from 0.004 wt. % to 0.141 wt. %. $\delta^{13}C_{TOC}$ values vary between −22.4 ‰ and −29.5 ‰ (average = −25.2 ‰), whereas TIC is more enriched in ^{13}C ($\delta^{13}C_{TIC}$ = −14.5 ‰ to −6.1 ‰; Table S-2). Carbonates derived from circulating unmodified seawater and the mantle typically have $\delta^{13}C$ values of approximately 0 and −7 ‰, respectively (Fig. 3; Deines, 2002). The low $\delta^{13}C_{TIC}$ values and their large shift in the SMT metamorphic rocks indicate that organic matter was oxidised into ^{12}C-enriched CO_2, which shifted the isotopic values of the dissolved inorganic carbon pool from which carbonate precipitated. Similar $\delta^{13}C_{TIC}$ values were also recorded in altered basalts on the Costa Rica Rift and attributed to microbial metabolic processes (Torsvik *et al.*, 1998). The $\delta^{13}C_{TOC}$ values recorded in the SMT metamorphic rocks are typically lower than $\delta^{13}C_{TOC}$ values (−17.5 to −21.3 ‰) of the surrounding sediments (Fig. 3b; Table S-2). This clearly indicates that the source of organic carbon in such rocks is different from those in the surrounding sediments. Abiotic organic synthesis in the oceanic lithosphere, including Fischer-Tropsch-type reactions (150–350 °C), re-speciation and high temperature reactions (>400–500 °C) of C-O-H fluids during magma cooling, and carbonate decomposition to CH_4 (<800 °C),

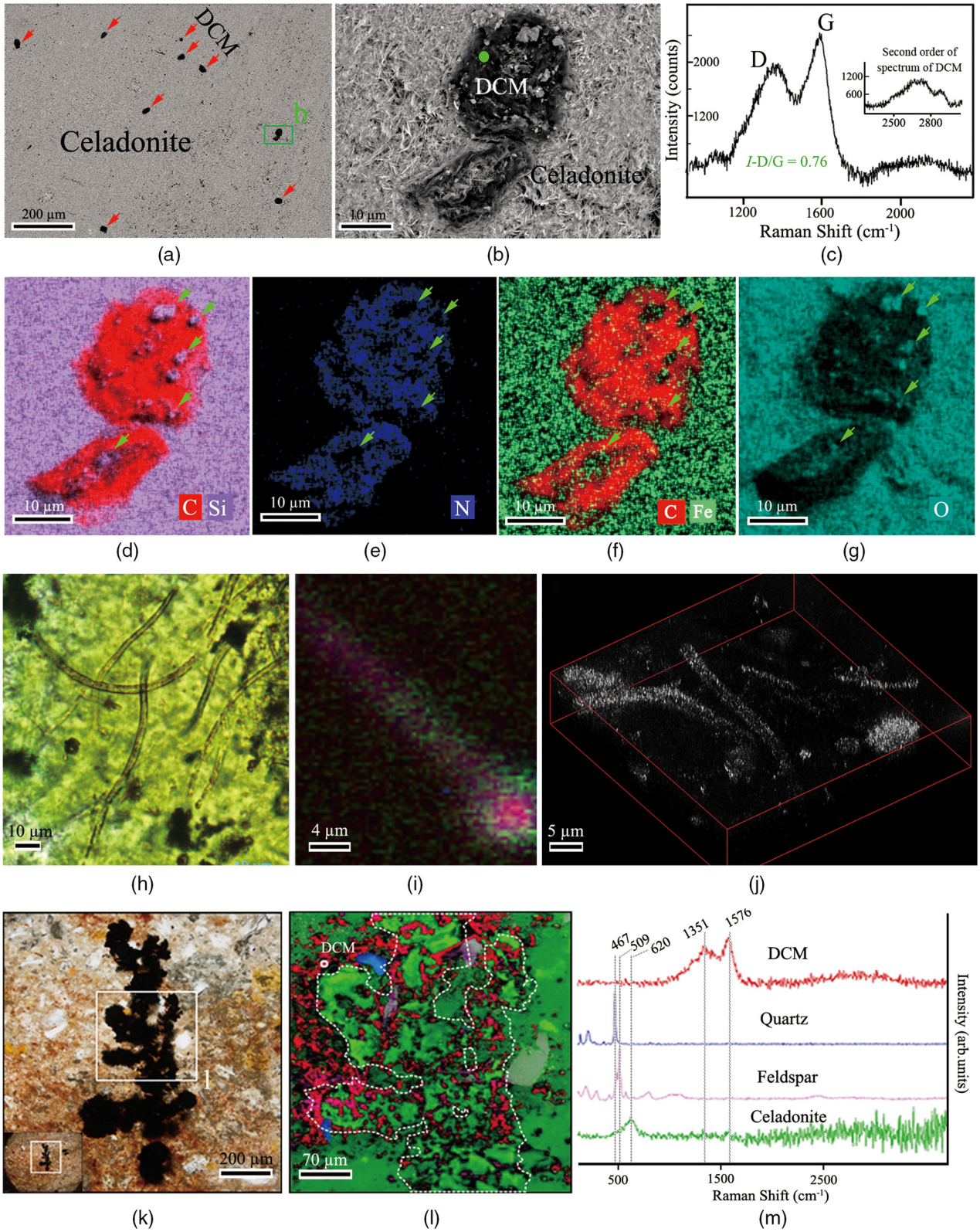

Figure 2 Representative carbonaceous spheroids (**a-g**; sample JL122-G01), filaments (**h-j**; sample JL122-G01), and *Frutexites*-like structures (**k-m**; sample JL122-G02) preserved in metamorphic rocks. **(a)** SEM-BSE image showing the distribution of spheroids composed of disordered carbonaceous matter (DCM, red arrows) in celadonite. **(b)** Enlarged view of DCM shown with a green rectangle in **(a)**. **(c)** Raman spectrum collected at location marked by a green spot in **(b)**, showing the characteristic first order (D band at ~1365 cm^{-1} and G band at ~1590 cm^{-1}) and second order (between ~2500 and 3000 cm^{-1}) bands of DCM. **(d–g)** SEM-EDS images corresponding to **(b)**, showing that DCM comprising of carbon (C) and nitrogen (N) is embedded by celadonite with celadonite grains on the inside (green arrows). **(h)** Transmitted white light photomicrograph of filaments. **(i)** Micro-Raman image of a filament. Reds and greens represent DCM and celadonite, respectively. **(j)** Three dimensional CLSM image of filaments using 488 nm laser excitation. **(k)** Transmitted white light photomicrographs of *Frutexites*-like structures. **(l)** Micro-Raman image of the white box shown in **(k)**. White dotted lines indicate the contour of *Frutexites*-like structure. Reds, greens, blues and pinks represent DCM, celadonite, quartz and feldspar, respectively. **(m)** Average Raman spectra of DCM and minerals from **(l)**.

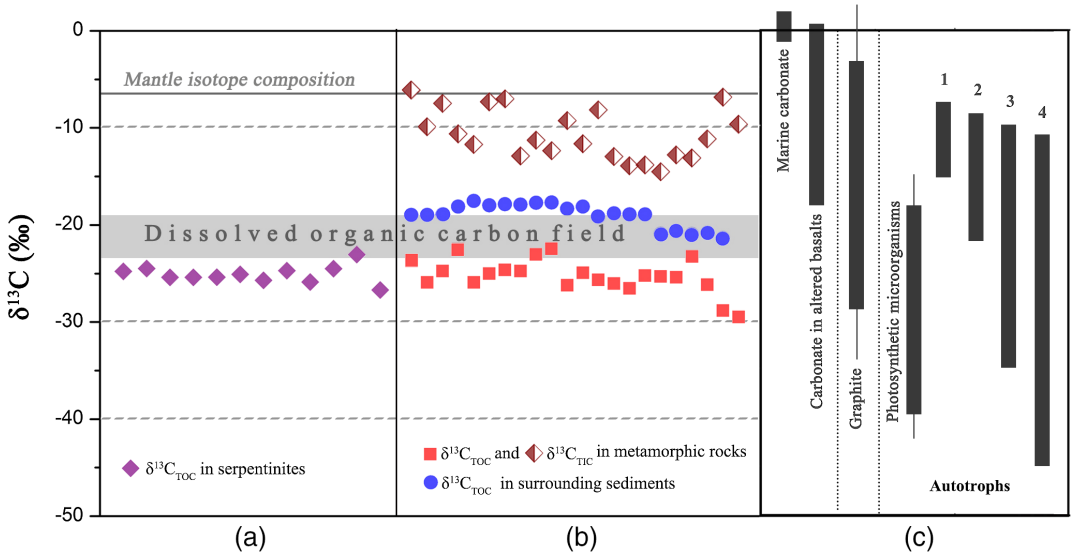

Figure 3 **(a)** Total organic carbon isotopes in serpentinites from Iberian Margin (Schwarzenbach *et al.*, 2013). **(b)** Carbon isotopes in zeolite-rich metamorphic rocks and surrounding sediments from the SMT. **(c)** Carbon isotope variations found in nature (Schidlowski, 2001). The right hand column shows carbon isotope fractionation variations in four different carbon fixation pathways by autotrophic microorganisms (1: 3-hydroxypropionate cycle; 2: reductive tricarboxylic acid (rTCA) cycle; 3: Calvin-Benson-Bassham cycle; 4: reductive acetyl-CoA pathway). Data for the dissolved organic carbon field are from Bauer (2002).

may also produce organic matter with a similar range of $\delta^{13}C$ values, but they dominantly form methane and short chain hydrocarbons (Andreani and Ménez, 2019) and their required temperatures are inconsistent with the low temperature (20–89 °C) zeolite facies rocks studied here. Although some evidence suggests abiotic carbonaceous matter can be formed during low temperature alteration of ocean crust (<150 °C), it would have a distinct chemical composition containing aromatic carbon and short aliphatic chains (Sforna *et al.*, 2018). Raman analysis shows that the intensity ratio of the D and G bands for DCM is 0.76 (Fig. 2c), which is distinctly higher than that for graphite from the Loch Maree Group (0.21), but falls within those for organic matter from the Applecross, Aultbea and Cailleach Head Formations (0.47–1.02; Muirhead *et al.*, 2016). This clearly indicates that such organic carbon in SMT metamorphic rocks is not graphite. Similar $\delta^{13}C_{TOC}$ values were found in serpentinite muds from mud volcanoes on the Mariana forearc (Eickenbusch *et al.*, 2019), and serpentinites from the Iberian Margin (Schwarzenbach *et al.*, 2013). Alongside an isotopic offset of TOC relative to marine dissolved organic carbon, Raman and lipid biomarker analyses provide strong evidence that such organic carbon is primarily derived from chemolithoautotrophic microorganisms instead of abiotic production (Schwarzenbach *et al.*, 2013; Klein *et al.*, 2015). Thus, carbon isotope data suggest that this organic carbon in SMT metamorphic rocks is of biological origin.

Glycerol dibiphytanyl glycerol tetraether lipids (GDGTs) analyses reveal that the GDGTs concentrations in the outer portions of metamorphic rocks (OPMR; GDGT-0: 5.445–8.784 ng/g; crenarchaeol: 14.527–17.427 ng/g; branched GDGT: 2.471–3.538 ng/g) are comparable to those of the surrounding sediments (GDGT-0: 4.939–11.385 ng/g; crenarchaeol: 10.783–26.826 ng/g; branched GDGT: 2.196–7.665 ng/g), but notably higher than those in the inner portions of metamorphic rocks (IPMR; GDGT-0: 0.086–0.800 ng/g; crenarchaeol: 0.012–0.192 ng/g; branched GDGT: 0.044–0.597 ng/g; Table S-3). Crenarchaeol is considered to be a specific biomarker for Thaumarchaeota that grows chemoautotrophically by utilising ammonium or other electron donors (Pester *et al.*, 2011), whereas GDGT-0 is most likely to be synthesised by both Thaumarchaeota and methanogenic archaea in deep subseafloor environments that grow chemoautotrophically by utilising H_2 (Weijers *et al.*, 2009). Crenarchaeol and branched GDGTs can be produced in subseafloor environments (Lincoln *et al.*, 2013; Pan *et al.*, 2016), even though they are commonly regarded as typical water column and soil biomarkers, respectively. In the OPMR, the GDGT-0 *vs.* crenarchaeol ratios (GCR; 0.4 to 0.5) are similar to those of the surrounding sediments (0.3–0.5), indicating that Thaumarchaeota is a preponderant group of Archaea (Fig. 4; Schouten *et al.*, 2002). In the IPMR, the GCR ranges from 1.4 to 59.5 indicating a substantial methanogenic source for GDGT-0 (Weijers *et al.*, 2009), as detected in Lost City chimneys and Iberia Margin brucite-calcite veins (Lincoln *et al.*, 2013; Klein *et al.*, 2015). In addition, the branched *vs.* isoprenoid tetraether (BIT) values for the IPMR range from 0.42 to 0.97, with an average value of 0.72 (n = 5; Fig. 4). These values are distinctly higher than those observed for the OPMR (average = 0.15, n = 2) and surrounding sediments (average = 0.19, n = 6), but almost identical to those observed for low temperature hydrothermal deposits (average = 0.63, n = 4; Pan *et al.*, 2016). Collectively, these tetraether lipid signatures further corroborate the *in situ* contribution of organic carbon by chemolithoautotrophic life in the IPMR.

H_2 generated by anaerobic basalt-fluid reactions during low grade metamorphism can function as an electron donor to provide energy for known chemolithoautotrophic life in metamorphic ocean crusts (Du *et al.*, 2019). Ferrous iron in basaltic minerals, such as pyroxene and olivine, can be oxidised to ferric iron through the dissociation of water during metamorphism and result in the generation of H_2 (Bach, 2016). Previous laboratory experiments demonstrated that H_2 could be generated through anaerobic basaltic mineral-water reaction at low to moderate temperatures (30 °C to 200 °C; Stevens and McKinley, 2000). High GCR ranging from 1.4 to 59.5 (Fig. 4), together with trace iron in zeolite facies rocks, strongly support this hypothesis. Besides H_2, ammonium could provide another potential electron donor for chemolithoautotrophic life in metamorphic rocks, as indicated by high contents of crenarchaeol and NH_4^+ (average = 8.8 ppm; Table S-4) in

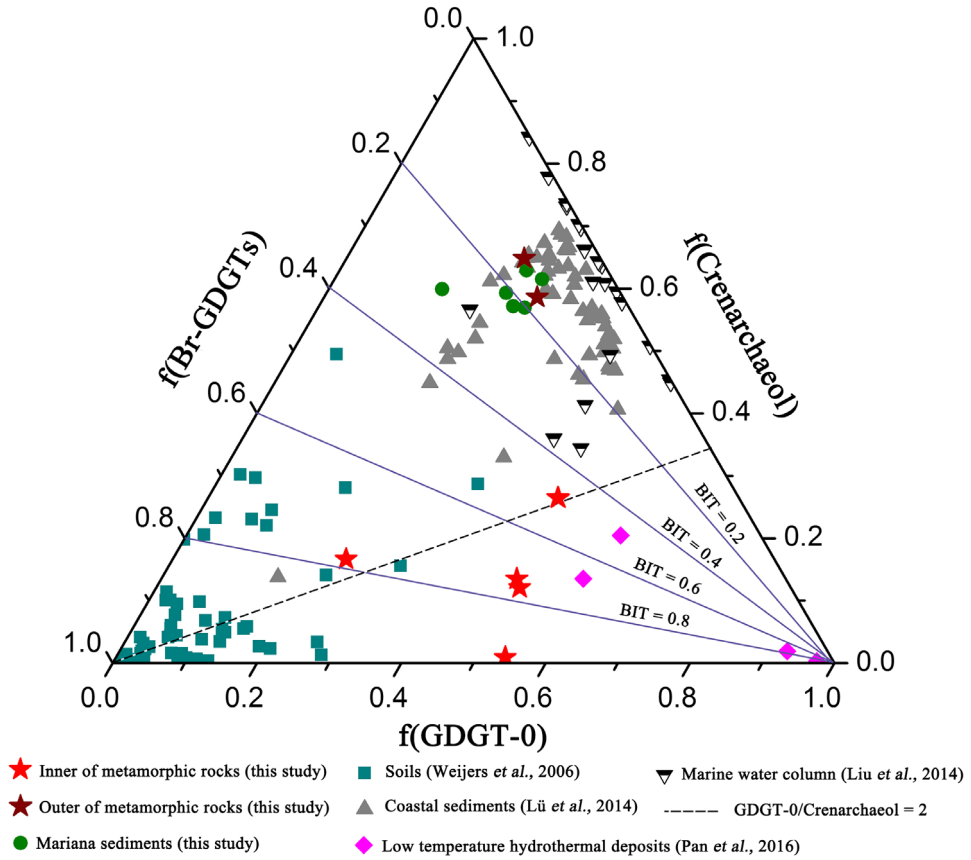

Figure 4 Ternary diagram showing the relationships of the fractional abundances of acyclic glycerol dibiphytanyl glycerol tetraether lipids (GDGT-0), crenarchaeol and sum of all branched GDGTs (Br-GDGTs) in different environments.

some of metamorphic rocks. Ammonia can be derived from the abiotic mineral catalysed reduction of N_2, NO_2^- and NO_3^- (Brandes *et al.*, 1998) or microbial nitrate reduction coupled with H_2 oxidation (Cowen *et al.*, 2003) in the upper ocean crust. These autotrophic metabolisms in the metamorphic crust may evolve during rock aging and decrease with decreasing intensity of fluid-rock reactions (Türke *et al.*, 2018).

The low grade metamorphic ocean crust described here represents previously underexplored habitats for chemolithoautotrophic life on Earth. From the P-T phase diagram (Fig. S-1), this habitable niche, with temperatures below the upper limit for life (122 °C; Takai *et al.*, 2008), is expected to extend up to approximately 14 km into the ocean lithosphere of the subduction zone, far deeper than either the known basalt-hosted deep biosphere that is dominant in the upper 300–500 m of the ocean crust (Furnes *et al.*, 2008), or the ultramafic rock-hosted deep biosphere that is predicted as deep as ~10 km below the seafloor (Plümper *et al.*, 2017). However, it still remains unclear how long this endolithic life was sustained and to what extent it impacts crustal biogeochemical cycles. Future works in other deep sea localities are needed to further comprehend this deep subsurface ecosystem and its potential role in the deep carbon cycle in the region scale geological context.

Acknowledgements

We are very grateful to the pilots and crew of the RV*XYH09-Jiaolong* for their professional service during the two cruises in June to July 2016 and in May to June 2017. Funding for this study was provided by the National key research and development plan of China (2018YFC0309902, 2018YFC0309802 and 2016YFC0302301) and the Doctoral Fund of Hebei Normal University (L2020B24). We acknowledge the Editor Prof. Liane G. Benning, as well as four anonymous reviewers, for their constructive comments that greatly improved the manuscript.

Editor: Liane G. Benning

Author Contributions

XP designed research. XP, ZG, MD, KT and HX participated in the cruise. XP, ZG, MD, KT, ADC, DP and HX performed research and analysed data. All authors discussed the results and wrote the paper. XP, ZG, and MD contributed equally to this work.

Additional Information

Supplementary Information accompanies this letter at http://www.geochemicalperspectivesletters.org/article2017.

Cite this letter as: Peng, X., Guo, Z., Du, M., Czaja, A.D., Papineau, D., Chen, S., Xu, H., Li, J., Ta, K., Bai, S., Dasgupta, S. (2020) Past endolithic life in metamorphic ocean crust. *Geochem. Persp. Let.* 14, 14–19.

References

Andreani, M., Ménez, B. (2019) New Perspectives on Abiotic Organic Synthesis and Processing during Hydrothermal Alteration of the Oceanic Lithosphere. In: Orcutt, B., Daniel, I., Dasgupta, R. (Eds.) *Deep Carbon: Past to Present*. Cambridge University Press, Cambridge, 447–479.

Bach, W. (2016) Some compositional and kinetic controls on the bioenergetics landscapes in oceanic basement. *Frontiers in Microbiology* 7, 1–8.

Bauer, J.E. (2002) In: Hansell, D.A., Carlson, C.A. (Eds.) *Biogeochemistry of Marine Dissolved Organic Matter: Carbon isotopic composition of DOM*. Academic Press, Cambridge, 405–455.

Brandes, J.A., Boctor, N.Z., Cody, G.D., Cooper, B.A., Hazen, R.M., Yoder Jr, H.S. (1998) Abiotic nitrogen reduction on the early Earth. *Nature* 395, 365–367.

Buick, R. (1990) Microfossil Recognition in Archean Rocks: An Appraisal of Spheroids and Filaments from a 3500 M.Y. Old Chert-Barite Unit at North Pole, Western Australia. *Palaios* 5, 441–459.

Cowen, J.P, Giovannoni, S.J., Kenig, F., Johnson, H.P., Butterfield, D., Rappe, M.S., Hutnak, M., Lam, P. (2003) Fluids from aging ocean crust that support microbial life. *Science* 299, 120–123.

Deines, P. (2002) The carbon isotope geochemistry of mantle xenoliths. *Earth-Science Reviews* 58, 247–278.

Du, M., Peng, X., Seyfried Jr, W.E., Ta, K., Guo, Z., Chen, S., Chou, I.M., Li, J., Xu, H. (2019) Fluid discharge linked to bending of the incoming plate at the Mariana subduction zone. *Geochemical Perspectives Letters* 11, 1–5.

Eickenbusch, P., Takai, K., Sissman, O., Suzuki, S., Menzies, C., Sakai, S., Sansjofre, P., Tasumi, E., Bernasconi, S.M., Glombitza, C., Jørgensen, B.B., Morono, Y., Lever, M.A. (2019) Origin of Short-Chain Organic Acids in Serpentinite Mud Volcanoes of the Mariana Convergent Margin. *Frontiers in Microbiology* 10, 1729.

Furnes, H., Mcloughlin, N., Muehlenbachs, K., Banerjee, N., Staudigel, H., Dilek, Y, De Wit, M., Van Kranendonk, M., Schiffman, P. (2008) Oceanic pillow lavas and hyaloclastites as habitats formicrobial life through time – a review. In: Dilek, Y., Furnes, H., Muehlenbachs, K. (Eds.) *Links Between Geological Processes, Microbial Activities and Evolution of Life*. Springer Verlag, Berlin, 1–68.

Heim, C., Queâric, N-V., Ionescu, D., Schaèfer, N., Reitner, J. (2017) Frutexites-like structures formed by iron oxidizing biofilms in the continental subsurface (Äspö Hard Rock Laboratory, Sweden). *PLoS ONE* 12, e0177542.

Ivarsson, M., Lindblom, S., Broman, C., Holm, N.G. (2008) Fossilized microorganisms associated with zeolite–carbonate interfaces in sub-seafloor hydrothermal environments. *Geobiology* 6, 155–170.

Klein, F., Humphris, S.E., Guo, W., Schubotz, F., Schwarzenbach, E.M., Orsi, W.D. (2015) Fluid mixing and the deep biosphere of a fossil Lost City-type hydrothermal system at the Iberia Margin. *Proceedings of the National Academy of Sciences of the United States of America* 112, 12036–12041.

Lincoln, S.A., Bradley, A.S., Newman, S.A., Summons, R.E. (2013) Archaeal and bacterial glycerol dialkyl glycerol tetraether lipids in chimneys of the Lost City Hydrothermal Field. *Organic Geochemistry* 60, 45–53.

Liu, X., Zhu, C., Wakeham, S.G., Hinrichs, K.-U. (2014) In situ production of branched glycerol dialkyl glycerol tetraethers in anoxic marine water columns. *Marine Chemistry* 166, 1–8.

Lü, X., Yang, H., Song, J., Versteegh, G.J.M., Li, X., Yuan, H., Li, N., Yang, C., Yang, Y., Ding, W., Xie, S. (2014) Sources and distribution of isoprenoid glycerol dialkyl glycerol tetraethers (GDGTs) in sediments from the east coastal sea of China: Application of GDGT-based paleothermometry to a shallow marginal sea. *Organic Geochemistry* 75, 24–35.

Marshak, S. (2009) *Essentials of Geology*. 3rd Edition, W.W. Norton, New York, ISBN: 978-0-393-93238-6.

Muirhead, D.K., Parnell, J., Spinks, S., Bowden, S.A. (2016) Characterization of organic matter in the Torridonian using Raman spectroscopy. In: Brasier, A.T., McIlroy, D., McLoughlin, N. (Eds.) *Earth System Evolution and Early Life: A Celebration of the Work of Martin Brasier*. Geological Society, London, Special Publications 448, 71–80.

Orsi, W.D. (2018) Ecology and evolution of seafloor and subseafloor microbial communities. *Nature Reviews Microbiology*, doi:10.1038/s41579-018-0046-8.

Pan, A.Y., Yang, Q.H., Zhou, H.Y., Ji, F.W., Wang, H., Pancost, R.D. (2016) A diagnostic GDGT signature for the impact of hydrothermal activity on surface deposits at the Southwest Indian Ridge. *Organic Geochemistry* 99, 90–101.

Pester, M., Schleper, C., Wagner, M. (2011) The Thaumarchaeota: an emerging view of their phylogeny and Ecophysiology. *Current Opinion in Microbiology* 14, 300–306.

Plümper, O., King, H.E., Geisler, T., Liu, Y., Pabst, S., Savov, I.P., Rost, D., Zack, T. (2017) Subduction zone forearc serpentinites as incubators for deep microbial life. *Proceedings of the National Academy of Sciences of the United States of America* 114, 4324–4329.

Schidlowski, M. (2001) Carbon isotopes as biogeochemical recorders of life over 3.8 Ga of Earth history: evolution of a concept. *Precambrian Research* 106, 17–134.

Schouten, S., Hopmans, E.C., Schefuss, E., Sinninghe Damste, J.S. (2002) Distributional variations in marine crenarchaeotal membrane lipids: a new tool for reconstructing ancient sea water temperatures? *Earth and Planetary Science Letters* 204, 265–274.

Schwarzenbach, E.M., Früh-Green, G.L., Bernasconi, S.M., Alt, J.C., Plas, A. (2013) Serpentinization and carbon sequestration: A study of two ancient peridotite-hosted hydrothermal systems. *Chemical Geology* 351, 115–133.

Sforna, M.C., Brunelli, D., Pisapia, C., Pasini, V., Malferrari, D., Ménez, B. (2018) Abiotic formation of condensed carbonaceous matter in the hydrating oceanic crust. *Nature Communications* 9, 5049.

Stevens, T.O., McKinley, J.P. (2000) Abiotic controls on H_2 production from basalt-water reactions and implications for aquifer biogeochemistry. *Environmental Science and Technology* 34, 826–831.

Takai, K., Nakamura, K., Toki, T., Tsunogai, U., Miyazaki, M., Miyazaki, J., Hirayama, H., Nakagawa, S., Nunoura, T., Horikoshi, K. (2008) Cell proliferation at 122 °C and isotopically heavy CH_4 production by a hyperthermophilic methanogen under high-pressure cultivation. *Proceedings of the National Academy of Sciences of the United States of America* 105, 10949–10954.

Torsvik, T., Furnes, H., Muehlenbachs, K., Thorseth, I.H., Tumyr, O. (1998) Evidence for microbial activity at the glass-alteration interface in oceanic basalts. *Earth and Planetary Science Letters* 162, 165–176.

Türke, A., Menez, B., Bach, W. (2018) Comparing biosignatures in aged basalt glass from North Pond, Mid-Atlantic Ridge and the Louisville Seamount Trail, off New Zealand. *PLoS ONE* 13, e0190053.

Weijers, J.W.H., Schouten, S., Spaargaren, O.C., Sinninghe Damsté, J.S. (2006) Occurrence and distribution of tetraether membrane lipids in soils: implications for the use of the TEX86 proxy and the BIT index. *Organic Geochemistry* 37, 1680–1693.

Weijers, J.W.H., Blaga, C.I., Werne, J.P., Sinninghe Damsté, J.S. (2009) Microbial membrane lipids in lake sediments as a paleothermometer. *PAGES news* 17, 102–104.

Geochemical Perspectives Letters

Past endolithic life in metamorphic ocean crust

X. Peng, Z. Guo, M. Du, A.D. Czaja, D. Papineau, S. Chen, H. Xu, J. Li, K. Ta, S. Bai, S. Dasgupta

Supplementary Information

The Supplementary Information includes:

- Materials and Methods
- Supplementary Text
- Tables S-1 to S-4
- Figures S-1 to S-9
- Video S-1
- Supplementary Information References

Materials and Methods

Sampling

The low-grade metamorphic rocks that have been tectonically extruded at the seafloor were recovered from the southern Mariana trench (SMT) (Table S-1), using manipulators of the manned submersible *Jiaolong* during two cruises of R/V XYH09 from June to July 2016 and from May to June 2017. After recovery, the rock samples were immediately placed in a biobox equipped on submersible *Jiaolong* to avoid potential contamination from seawater. Sediments were collected with push-core samplers. Once on deck, metamorphic rocks and sediment samples were immediately subsampled and stored at -20 °C or -80 °C until further analysis.

X-ray diffraction analysis

Mineral compositions were determined using Cu Kα radiation on a Bruker D8 Advance X-ray diffractometer, which was operated at 40 kV and 40 mA with a scanning speed of 2°/min between 3° and 70° at Guangzhou Institute of Geochemistry, Chinese Academy of Sciences. Prior to X-ray diffraction (XRD) analysis, small pieces of the analysed metamorphic rocks were ultrasonicated in deionised water, freeze-dried under anoxic conditions to avoid oxidation during drying and then thoroughly ground using a pestle and mortar.

Scanning electron microscopy

Back-scattered electron (BSE) images of rock chips were collected using a FEI Quanta FEG 250 high-resolution field emission

scanning electron microscopy (SEM) equipped with an EDAX energy dispersive X-ray spectroscopy (EDS) analysis system at FEI Trading (Shanghai) Co. Ltd (China). SEM was operated at 5 or 10 kV with a working distance of 10 mm to provide optimal imaging and minimise charging and sample damage in the BSE imaging mode. An accelerating voltage of 20 kV was used for the X-ray analysis to acquire elemental distributions.

Nano-scale secondary ion mass spectrometry

Elemental maps were performed on the polished 30-μm-thick thin sections using a Cameca NanoSIMS 50L (CAMECA, Paris, France) at the Institute of Geology and Geophysics, Chinese Academy of Sciences, following the procedure previously described (Peng *et al.*, 2016). Each region of interest was pre-sputtered with a 150 pA beam current and an ion dose of N =5 × 10^{16} ions/cm^2 to remove the conductive coating (Au) and the contaminants that were generated during pretreatment. In the multi-collection mode, negative secondary ions ($^{12}C^-$, $^{12}C^{14}N^-$, $^{28}Si^-$, $^{31}P^-$, $^{32}S^-$, $^{24}Mg^{16}O^-$, and $^{56}Fe^{16}O^-$) were sputtered from the sample surface using a Cs^+ primary beam with ~2.5 pA intensity. All of the images referred to in this paper are 256 × 256 pixels, recorded in ~30 min.

Raman spectrometry

Rock chips were analysed using a LabRAM HR Evolution (Horiba Jobin Yvon) confocal Raman spectrometer equipped with a 532 nm excitation laser at the Institute of Deep-sea Science and Engineering, Chinese Academy of Sciences. Individual spectra were recorded using 50 × objective lens, ~1 μm diameter analysing spot area, ~3 mW laser power, and 10 s × 2 measuring sequence. The analytical methods were described elsewhere (Guo *et al.*, 2018). Micro-Raman imaging was performed primarily on polished thin sections with the a300 WITec confocal laser scanning micro-spectroscopy system at the University College of London (UCL), using a 532 nm laser tuned at 12 mW coupled to an inverted optical microscope by an optical fiber, according to previously described techniques (Papineau *et al.*, 2017). In brief, a 50 microns diameter optic fiber is used to harvest the inelastically scattered photons. A 100 × objective is used to provide a spatial resolution between 500 and 360 nm in the Raman images, whereas a 600 lines/mm grating is used to obtain spectra with a spectral resolution around 4 cm^{-1}. Raman hyperspectral images of mineral associations were generated by mapping the main peak intensities for specific minerals using the WITec Project Four Plus data processing software; the peaks include those distinct for quartz (~467 cm^{-1}), feldspar (~509 cm^{-1}), celadonite (~620 cm^{-1}), and carbonaceous matter (~1576 cm^{-1}). All Raman peak positions were read directly from measured average spectra calculated from representative regions with high signal-to noise and after background removal.

Confocal laser scanning microscopy

Microfossil structures were located and photographed within the polished thin sections using a Leica DM2700P polarising light microscopy in transmitted white light with a wavelength of 550 nm. Two- and three-dimensional fluorescence images of selected specimens were acquired with an Olympus Fluoview 1200 confocal laser scanning microscopy (CLSM; Olympus, Inc., Shinjuku, Japan) running the FV10-ASW software (v. 3.01) at the University of Cincinnati, following the procedure previously described (Guo *et al.*, 2018). No stains were used on the samples because the filamentous structures of interest are embedded in a mineral matrix, and thus, the CLSM images are based on autofluorescence. The CLSM was operated at 488 nm laser excitation, a 60 × oil-immersion objective (NA [numerical aperture] = 1.42) with fluorescence-free microscopy immersion oil (Olympus Type-F), and a 505-605 nm bandpass filter to exclude the incident laser wavelength. The 2-D images were exported as TIF files and then rendered into 3-D images by use of the software program Paraview v. 5.0.1 (Kitware Inc., Clifton Park, NY).

Carbon and oxygen isotope compositions

Analyses of carbon and oxygen isotope compositions were carried out from bulk rock powders and surrounding sediments at the

Stable Isotope Laboratory, Third Institute of Oceanography, State Oceanic Administration, China. Total inorganic carbon (TIC) was determined using Gas Bench II–IRMS by extracting CO_2 from ~100 μg of powdered sample treated with 100% orthophosphoric acid. Total organic carbon (TOC) was determined using Element Analyzer (Flash EA 1112 HT) after removing carbonate. Total carbon (TC) was calculated by adding TIC and TOC. Reproducibility for TIC and TOC were approximately 0.3 %. The $\delta^{13}C_{TOC}$, $\delta^{13}C_{TIC}$ and $\delta^{18}O_{CaCO3}$ values were analysed using the stable isotope mass spectrometer (Thermo Delta V Advantages). Carbon isotope values are reported as standard δ-notation (in units of per mil, ‰), relative to the Vienna Pee Dee Belemnite (VPDB) standard. They were calculated according to the following equation:

$$\delta^{13}C\ (‰) = [(^{13}C/^{12}C)_{sample} / (^{13}C/^{12}C)_{VPDB} - 1] \times 1000 \quad \text{Eq. S-1}$$

where $(^{13}C/^{12}C)_{VPDB}$ is the carbon isotope ratio of VPDB. The analytical accuracy of the $\delta^{13}C$ values was better than ±0.2‰.

Oxygen isotope values are reported as standard δ-notation (in units of per mil, ‰), relative to the SMOW standard. They were calculated according to the following equation:

$$\delta^{18}O\ (‰) = [(^{18}O/^{16}O)_{sample} / (^{18}O/^{16}O)_{SMOW} - 1] \times 1000 \quad \text{Eq. S-2}$$

where $(^{18}O/^{16}O)_{SMOW}$ is the oxygen isotope ratio of SMOW. The analytical accuracy of the $\delta^{18}O$ values was better than ±0.2 ‰.

Staining

Thin sections were stained with the 4, 6-diamidino-2-phenylindole (DAPI) stain and examined by epifluorescence microscopy, following the procedure previously described (Fisk *et al.*, 2006). The petrographic thin section was rinsed with 10 ml of 75 % (vol/vol) ethanol, air-dried in a clean hood for 5 min, and then submerged in a 1:500 dilution of filter-sterilised (0.2 μm pore size) 0.1% (wt/vol) DAPI, which was dissolved in autoclaved phosphate-buffered saline solution (PBS; pH adjusted to 7.4). The petrographic thin section was subsequently subjected to the pressure from 1 atmosphere to partial vacuum (3.3 kPa for 2 min) after which the sample was incubated with the dye at 37 °C for 0.5 h. Following incubation, the thin section was rinsed with repeated washes of 50 ml of filter-sterilised PBS buffer. To remove unbound stain, the thin section was also cycled to partial vacuum and back to atmospheric pressure during washing. The thin section was imaged using an epifluorescence microscopy (Leica DM6B), which was operated at filter system for blue excitation with a 450-490 nm excitation filter, a 510 nm dichromatic mirror, and a 515 nm suppression filter.

Lipid analysis

The selected rocks were divided carefully into the inner and outer portions using a sterilised scoop cleaned with dichloromethane (Fig. S-9). Then, rock and sediment samples were grounded into powder using an agate pestle and mortar after freeze-drying. Approximately 15 g of the powder was extracted ultrasonically with a mixture of methanol (MeOH), dichloromethane and phosphate buffer at pH 7.4 (1:1:0.8, v/v, ×4) using a modified Bligh and Dyer method (Sturt *et al.*, 2004). After separation into an organic phase and an aqueous phase by centrifugation at 2500 rpm for 10 min, the bottom dichloromethane phase was collected using a glass pipette (×3), dried under a stream of nitrogen gas and then redissolved in 500 μl of hexane : dichloromethane 70:30 mixture.

Total lipids were separated into hydrocarbons, neutral lipids, and phospholipids using miniature silicic acid columns (Supelco Inc., Bellefonte, Pennsylvania, U.S.A.) eluted sequentially with 5 ml of hexane, chloroform, and methanol, respectively. The hydrocarbon (HC) fraction was dried in a gentle stream of nitrogen and resuspended in dichloromethane for GC-MS analysis. The neutral lipid (NL) fractions were dried under a stream of nitrogen, derivatised by adding 60 μl of N, O-bis (trimethylsilyl)-trifloroacetamide, and heated at 65°C for 40 min to produce trimethylsilyl ethers of sterols and alcohols (Fang *et al.*, 2007). 5α-

cholestane was used as an internal standard for quantification. Phospholipid fraction was subjected to a mild alkaline trans-methylation procedure to produce fatty acid methyl esters (FAME) (Fang *et al.*, 1996).

All the lipids were analysed on an Agilent 6890 Gas Chromatograph (GC) interfaced with an Agilent 5973 N Mass Selective Detector. Analytical separation of lipids was accomplished using a 30 m × 0.25 mm (internal diameter) DB-5 fused-silica capillary column (J&W Scientific, Folsom, California, U.S.A.). Column temperature was programmed from 50 to 120 °C at 10 °C min^{-1}, then to 310 °C at 5 °C min^{-1}, and held at 310 °C for 20 min. Lipids were identified based on mass spectra. Concentrations of lipids were obtained based on the gas chromatograph-mass spectrometer (GC-MS) response relative to that of an internal standard—C18 fatty acid ethyl ester for fatty acids and 5α-cholestane for hydrocarbons and neutral lipids. However, lipid biomarker (HC, NL, FAME) failed to be detected in our samples.

For analysis of glycerol dialkyl glycerol tetraether (GDGTs), C_{46} GDGT was added as internal standard to a part of the total lipid extract, dried under a stream of nitrogen gas, dissolved in hexane/isopropanol (99:1, v/v) and then passed through 0.45-μm polytetrafluoroethylene filters.

The GDGTs were analysed using an Agilent 1200 high performance liquid chromatography (HPLC) device connected to an Agilent 6460 triple quadrupole mass spectrometer, following the procedure described in Xie *et al.* (2015). The GDGT compounds were separated using an Alltech Prevail Cyano column (150 mm× 2.1 mm, 3 μm) at 30°C. The injection volume was 10 μl. For the first 5 min, GDGTs were eluted isocratically with n-hexane/isopropanol (99:1, v/v), followed by a linear gradient to 1.8% hexane/isopropanol (90:10, v/v) in 45 min. The flow rate was maintained at 0.2 ml/min. The column was cleaned by back flushing hexane/propanol (90:10, v/v) at 0.2 ml/min for 10 min after each analysis. The GDGTs (m/z 1302, 1300, 1298, 1296, 1294, 1292, 1018, 1020, 1022, 1032, 1034, 1036, 1046, 1048 and 1050) and C_{46} GDGT internal standard (m/z 744) were quantified by integration of peak areas from the extracted ion chromatograms.

The GDGTs membrane lipids of prokaryotes include archaeal isoprenoidal GDGTs (IsoGDGTs) and bacterial branched GDGTs (BrGDGTs). They have been widely used for tracing the sources of organic matter due to the difference in BrGDGTs and IsoGDGTs (Schouten *et al.*, 2013; Weijers *et al.*, 2014). Based on BrGDGTs and crenarchaeol (representative of marine IsoGDGTs) membrane lipids, the branched vs. isoprenoid tetraether (BIT) index was calculated following the equation of Hopmans *et al.* (2004):

$$\text{BIT index} = \frac{\text{GDGT I} + \text{GDGT II} + \text{GDGT III}}{\text{GDGT I} + \text{GDGT II} + \text{GDGT III} + \text{Crenarchaeol}} \quad \text{Eq. S-3}$$

Ammonium contents

Ammonium was extracted using the HF digestion and distillation technique, following the procedure previously described (Hall, 1993). Approximately 200–300 mg of the dried sample powders were weighed into PTFE bottles and then digested using 2 ml of 40% HF. The duration of the digestion was at least 7 days at room temperature, with the samples gently shaken on a regular basis. After digestion, about 20 ml of 25 % KOH solution was added to raise the pH, and the whole solution was distilled using a Kjeldahl apparatus until 15 ml of distillate had been collected in a 15 ml 0.01 N HCl solution. The amount of NH_4^+ was determined by colorimetry with phenol and sodium hypochlorite. Each sample was digested and analysed in triplicate, with a relative error of less than 10%.

Thermodynamic calculations

The amount of metabolic energy that is potentially available to a microorganism from a chemical reaction are calculated using the equation

$$\Delta G = \Delta G^\circ + RT \ln Q \quad \text{Eq. S-4}$$

where ΔG° represents the standard free energy, ΔG is the free energy, T is the temperature in Kelvin, and R is the universal gas constant, and Q stands for the activity product of the species involved in the reaction. Autotrophic hydrogen oxidation proceeds according to the reaction

$$4H_2 + CO_2 = CH_4 + 2H_2O \quad \text{Eq. S-5.}$$

Autotrophic ammonium oxidation proceeds according to the reaction

$$5NH^{4+} + 3NO_3^- = 4N_2 + 9H_2O + 2H^+ \quad \text{Eq. S-6.}$$

We assume that H_2 is generated through the alteration of pyroxene that accounts for 59 % of basaltic rocks. H_2 generation in pyroxene is calculated according to the equation:

$$4CaMg_{0.5}Fe_{0.5}Si_2O_6 + 10H^+ + 10H_2O = MgFe_2Si_3O_{10}.4H_2O + 5H_4SiO_4 + Mg^{2+} + 4Ca^{2+} + H_2 \quad \text{Eq. S-7.}$$

NH_4^+ contents in metamorphic rocks are used to calculate the amount of energy by autotrophic ammonium oxidation. It is also assumed that chemolithoautotrophs require 292 kJ to fix 1 g of biomass.

Supplementary Text

Frutexites-like structures

These arborescent structures branch off from main stems and have rounded terminations. Micro-Raman mapping shows that they contain μm-scale quartz, feldspar, celadonite and carbonaceous matter (Fig. 2l). Carbonaceous matter commonly occur as bulbous filaments that branch and vary from several hundreds of microns to up to 5 millimeters in length. Small carbonaceous grains also form discontinuous trails and disseminations on the surroundings of the *Frutexites*-like structures (Fig. 2k,l). These biogenic structures are distinctly different from abiogenic dendrites of Mn-oxide (Xu *et al.*, 2010) because they contain abundant carbonaceous matter and no Mn detected by SEM-EDS.

Lipid biomarkers

To further demonstrate the *in situ* production of organic carbon, we conducted lipid analyses of the inner and outer portions of metamorphic rocks. Only tetraether lipids were detected (Table S-3); no hydrocarbons, neutral lipids or fatty acid methyl esters were detected in these metamorphic rocks. Because the latters are common in seawater, this indicates that potential seawater or any other form of contamination was minimal.

Bioenergetic calculations

We use bioenergetic calculations based on redox reactions between H_2 and CO_2, as well as NH_4^+ and NO_3^-, to provide preliminary estimates of the potential energy that is available for *in situ* biomass production within low-grade metamorphic crust. Despite the existence of uncertainties, these calculations indicate the energy yielded by the reactions in 1 g metamorphic rock might support the production of 2.18×10^{-4} g of biomass associated with methanotrophy and 6.69×10^{-7} g of biomass associated with anaerobic ammonium oxidation, the total of which falls within the range of TOC content (0.008 wt. % to 0.379 wt. %) of metamorphic rocks.

Supplementary Tables

Table S-1 Location information and mineralogy characterisation of the metamorphic rocks and surrounding sediments in the subduction zone of the SMT.

Sample ID	Samples	Depth (mbsla)	Latitude N	Longitude E	Sample methods	Mineral composition
JL118-G03		6695	11.580°	141.883°	Jiaolong dive	Analcite, Chabazite, feldspar, chlorite
JL118-G04		6692	11.581°	141.882°	Jiaolong dive	Heulandite, mordenite, gismondine, maghemite
JL118-G06		6694	11.581°	141.882°	Jiaolong dive	Analcite, gmelinite, chabazite
JL119-G01		5997	11.665	142.250	Jiaolong dive	Phillipsite, plagioclase, gmelinite, illite, quartz, maghemite
JL119-G02	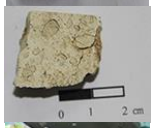	6001	11.665°	142.249°	Jiaolong dive	Phillipsite, plagioclase, gmelinite, maghemite
JL120-G01		6706	11.583°	141.878°	Jiaolong dive	Analcite, phillipsite, gmelinite, hematite
JL120-G02		6702	11.583°	141.878°	Jiaolong dive	Analcite, phillipsite, gmelinite, talc, hematite
JL120-G03		6705	11.583°	141.878°	Jiaolong dive	Heulandite/clinoptilolite, magnetite
JL121-G01		5590	11.799°	142.113°	Jiaolong dive	Phillipsite, plagioclase, quartz, maghemite
JL121-G04		5552	11.800°	142.116°	Jiaolong dive	Phillipsite, Labradorite, chlorite, quartz, maghemite
JL122-G01		6296	10.890°	142.227°	Jiaolong dive	Celadonite, ilmenite
JL122-G02		6296	10.890°	142.227°	Jiaolong dive	Celadonite, augite, ilmenite
JL144-G03		6304	10.889°	142.227°	Jiaolong dive	Natrolite, maghemite, labradorite, augite
JL145-G02		6531	11.630°	142.144°	Jiaolong dive	Phillipsite, natrolite, ferripyrophyllite

JL146-G01		6697	10.920°	141.696°	Jiaolong dive	Phillipsite, gmelinite, labradorite, maghemite
JL146-G02		6685	10.920°	141.696°	Jiaolong dive	Phillipsite, gmelinite, labradorite, maghemite
JL146-G05		6406	10.909°	141.704°	Jiaolong dive	Phillipsite, muscovite, labradorite, clinochlore, ferrihydrite
JL147-G03		6684	10.961°	141.983°	Jiaolong dive	Phillipsite, gmelinite, labradorite, chlorite
JL147-G06		6053	10.957°	141.986°	Jiaolong dive	Phillipsite, natrolite, plagioclase, clinochlore
JL147-G07		6053	10.957°	141.986°	Jiaolong dive	Phillipsite, muscovite, plagioclase, clinochlore, maghemite
JL147-G08		6053	10.957°	141.986°	Jiaolong dive	Natrolite, plagioclase, augite, maghemite
JL147-G10		6053	10.957°	141.986°	Jiaolong dive	Natrolite, labradorite, augite, magnetite
JL120-S01		6707	11.582°	141.879°	Push-core sampler	Analcite, plagioclase, quartz, clinochlore
JL121-S01		5569	11.800°	142.115°	Push-core sampler	Gismondine, plagioclase, quartz, clinochlore
JL122-S01		6329	10.889°	142.228°	Push-core sampler	Phillipsite, muscovite, plagioclase, quartz, clinochlore

[a] mbsl means meters beneath sea level.

Table S-2 Geochemical characterisation of the metamorphic rocks in the subduction zone of the SMT.

Sample ID	TOC [a] (wt. %)	TIC [b] (wt. %)	TC [c] (wt. %)	$\delta^{13}C_{TOC}$ (‰VPDB)	$\delta^{13}C_{TIC}$ (‰VPDB)	$\delta^{18}O$ [d] (‰SMOW)	Temperature [e] (ºC; -4‰ fluid)
JL118-G03	0.013	0.012	0.025	-23.7	-6.1	25.3	20
JL118-G04	0.008	0.004	0.012	-25.9	-9.9	20.4	44
JL118-G06	0.011	0.011	0.022	-24.7	-7.5	21.8	36
JL119-G01	0.046	0.014	0.060	-22.5	-10.6	14.0	88
JL119-G02	0.016	0.007	0.023	-25.9	-11.7	14.2	86
JL120-G01	0.013	0.006	0.020	-25.0	-7.3	21.3	39
JL120-G02	0.018	0.006	0.023	-24.6	-7.0	24.3	24
JL120-G03	0.013	0.009	0.022	-24.7	-12.9	14.0	89
JL121-G01	0.026	0.007	0.032	-23.0	-11.3	14.7	82
JL121-G04	0.034	0.08	0.042	-22.4	-12.3	14.0	88
JL122-G01	0.020	0.005	0.025	-26.2	-9.3	20.6	43
JL122-G02	0.013	0.005	0.018	-24.9	-11.6	13.9	89
JL144-G03	0.090	0.031	0.122	-25.2	-8.2	-	-
JL145-G02	0.261	0.141	0.402	-26.0	-13.0	-	-
JL146-G01	0.296	0.116	0.411	-26.5	-13.9	-	-
JL146-G02	0.379	0.039	0.418	-25.2	-13.8	-	-
JL146-G05	0.025	0.104	0.129	-25.3	-14.5	-	-
JL147-G03	0.032	0.114	0.147	-25.4	-12.8	-	-
JL147-G06	0.037	0.067	0.104	-23.2	-13.1	-	-
JL147-G07	0.032	0.075	0.107	-26.1	-11.1	-	-
JL147-G08	0.010	0.043	0.053	-28.8	-6.8	-	-
JL147-G10	0.013	0.054	0.067	-29.5	-9.7	-	-
Average	0.064	0.040	0.104	-25.2	-10.7	18.2	61

[a] Total organic carbon.
[b] Total inorganic carbon.
[c] Total carbon calculated by adding TIC and TOC.
[d] Oxygen isotope composition of carbonates extracted from metamorphic rocks.
[e] The temperature was estimated by the algebraic equation described previously:

$$1000\ln a = 2.78 \times (10^6 T^{-2}) - 3.39$$

where the fractionation factor a = ($^{18}O/^{16}O$)$CaCO_3$ / ($^{18}O/^{16}O$)fluid, and we assumed equilibrium with ^{18}O-depleted fluids (-4 ‰, SMOW) resulted from low-temperature reaction of seawater with basalt (Alt *et al.*, 1986).

Table S-3 The GDGTs concentrations (ng/g extract) of metamorphic rocks and sediments from the SMT.

Sample ID		GDGT-0	GDGT-1	GDGT-2	GDGT-3	Crenarchaeol	br-GDGT-III	br-GDGT-IIIb	br-GDGT-IIIc	br-GDGT-II	br-GDGT-IIb	br-GDGT-IIc	br-GDGT-I	br-GDGT-Ib	br-GDGT-Ic	∑Br-GDGT	BIT
		1302	1300	1298	1296	1292	1050	1048	1046	1036	1034	1032	1022	1020	1018		
JL121-G04-1 (Inner)	rocks	0.195	0.011	0.007	0.001	0.135	0.247	0.024	0.018	0.103	0.014	0.007	0.053	0.013	0.004	0.483	0.75
JL121-G04-2 (Outer)	rocks	5.445	0.154	2.107	0.120	14.527	1.621	0.017	0.016	0.298	0.033	0.000	0.414	0.050	0.023	2.471	0.14
JL120-G02 (Inner)	rocks	0.086	0.004	0.003	0.000	0.047	0.017	0.004	0.000	0.009	0.003	0.000	0.009	0.002	0.002	0.044	0.42
JL121-G01 (Inner-1)	rocks	0.693	0.439	0.526	0.019	0.012	0.239	0.032	0.148	0.021	0.000	0.000	0.131	0.005	0.004	0.581	0.97
JL121-G01 (Inner-2)	rocks	0.800	0.011	0.005	0.002	0.192	0.355	0.000	0.000	0.157	0.000	0.000	0.085	0.000	0.000	0.597	0.76
JL122-G02-1 (Inner)	rocks	0.297	0.009	0.004	0.001	0.081	0.126	0.006	0.004	0.048	0.006	0.000	0.035	0.000	0.000	0.225	0.72
JL122-G02-2 (Outer)	rocks	8.784	2.123	2.735	0.147	17.427	2.507	0.016	0.018	0.415	0.027	0.017	0.455	0.056	0.025	3.538	0.16
JL121 0-2	sediments	6.478	1.914	2.296	0.153	13.846	1.429	0.038	0.024	0.283	0.048	0.016	0.274	0.059	0.026	2.196	0.13
JL121 11-12	sediments	11.385	3.136	4.649	0.310	22.633	3.787	0.100	0.049	0.694	0.105	0.039	0.792	0.139	0.057	5.762	0.19
JL122 15-16	sediments	5.317	1.632	2.316	0.137	12.653	2.115	0.039	0.018	0.469	0.113	0.036	0.493	0.070	0.028	3.381	0.20
JL120 23-24	sediments	11.035	3.108	4.578	0.320	26.826	3.080	0.044	0.031	0.595	0.075	0.033	0.760	0.113	0.051	4.784	0.14
JL120 11-12	sediments	5.082	1.292	1.524	0.436	10.783	1.952	0.029	0.020	0.371	0.037	0.017	0.474	0.070	0.031	2.999	0.21
JL114 0-2	sediments	4.939	1.253	2.015	0.718	18.835	4.453	0.132	0.133	1.160	0.153	0.074	1.236	0.182	0.143	7.665	0.27
Blank-1		0	0	0	0	0	0	0	0	0	0	0	0	0	0	0	
Blank-2		0	0	0	0	0	0	0	0	0	0	0	0	0	0	0	

Table S-4 Comparison of ammonium (NH_4^+) contents in basalts and metamorphic rocks

Rock type	Sample ID	NH_4^+ contents (ppm)
Basalts	JL116-G02	0.78
	JL116-G04	1.35
Metamorphic rocks	JL120-G01	7.49
	JL122-G01	7.16
	JL122-G02	11.82

Supplementary Figures

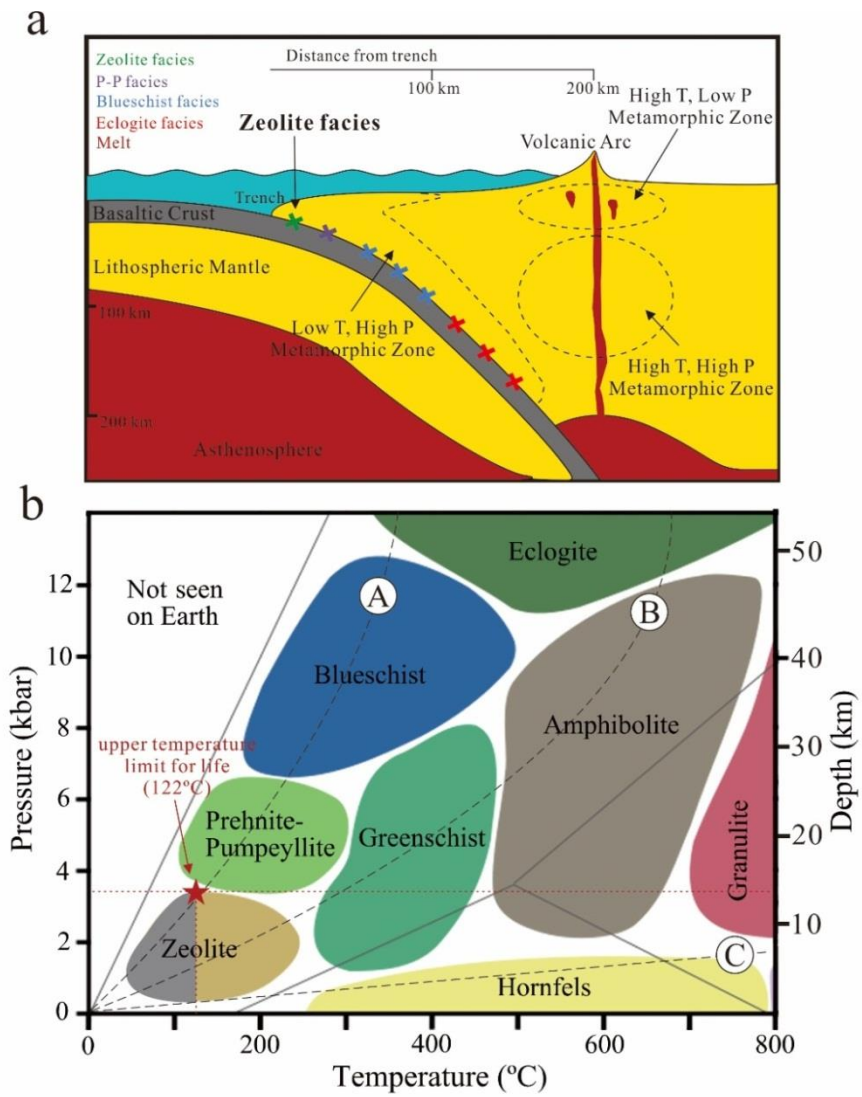

Figure S-1 Representative metamorphic zones and facies diagram. **(a)** Metamorphic zones near plate margins (modified from Winter, 2010), showing subduction zone metamorphism is characterised by a metamorphic path through zeolite, prehnite-pumpellyite (P-P), blueschist, and eclogite facies stability zones of subducted oceanic crust. **(b)** Metamorphic facies in pressure-temperature (P-T) diagram (modified from Marshak, 2009). Curve A represents a low geothermal gradient (Low T, High P), such as subduction zone metamorphism. Curve B represents a normal geothermal gradient (High T, High P), such as regional metamorphism. Curve C represents a high geothermal gradient (High T, Low P), such as contact metamorphism. Note that zeolite-facies rocks are first metamorphosed from basaltic rocks at depths of 1-14 km beneath the seafloor and temperatures of approximately 40-300 °C, part of which is well within the tolerance of life (<122 °C), as indicated by grey area.

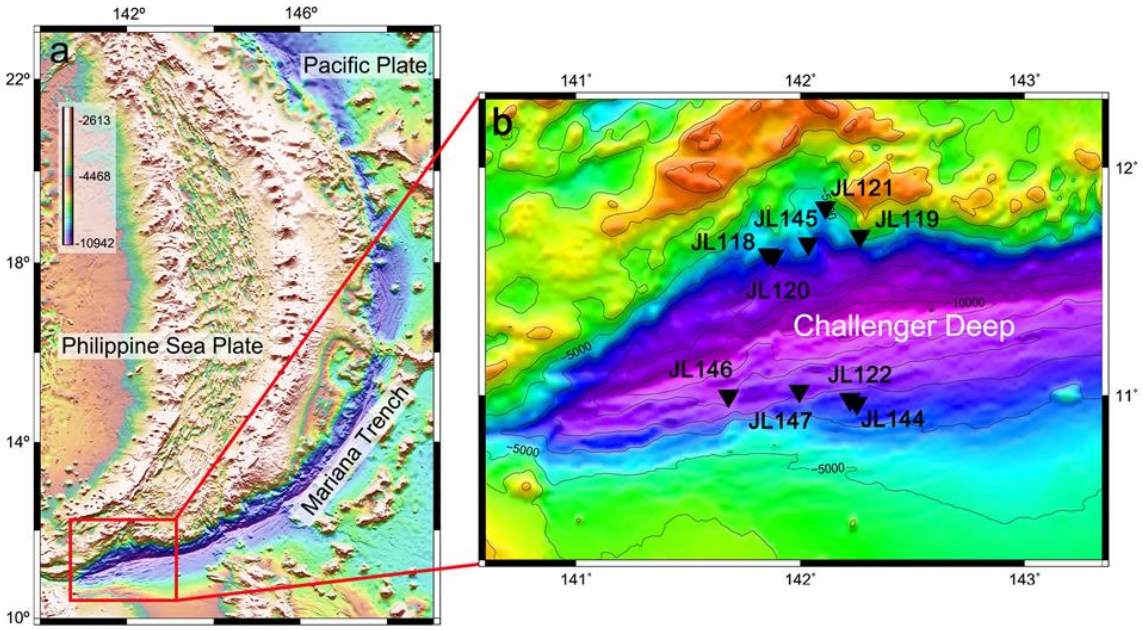

Figure S-2 (a) Color bathymetry map of the Philippine Sea region of the western Pacific displaying the location of the SMT (red box). **(b)** Enlarged map of the SMT with Jiaolong dive sites (black triangles).

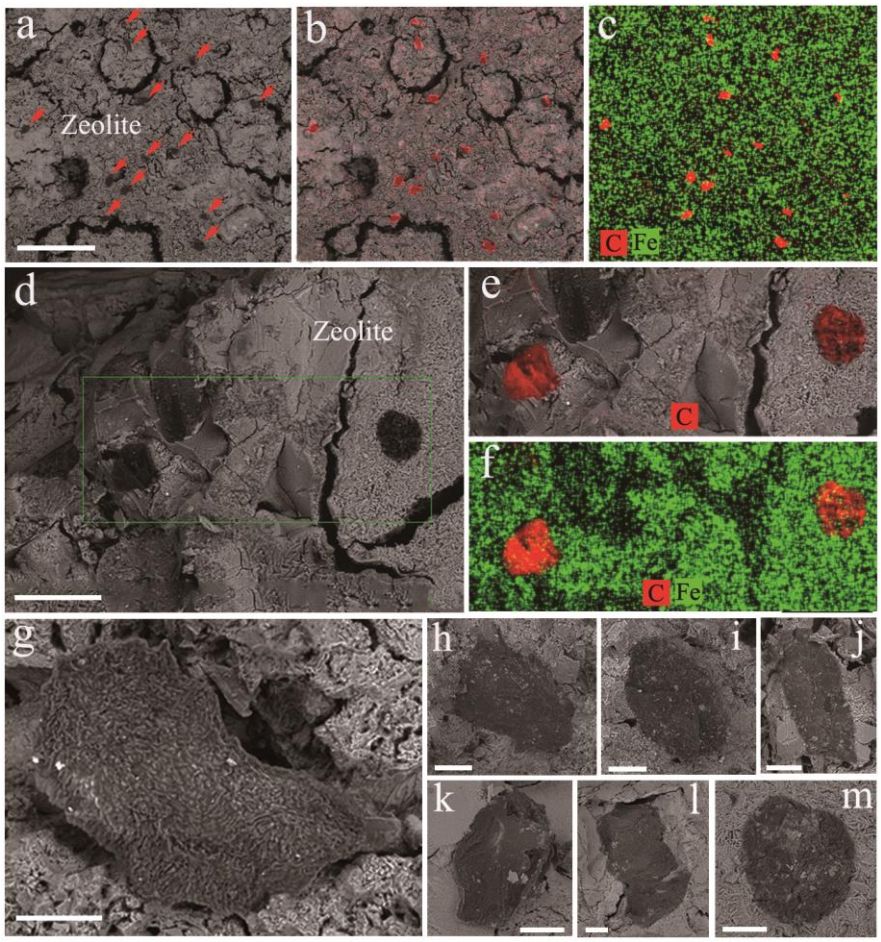

Figure S-3 Representative disordered carbonaceous matter (DCM) embedded in zeolite from the metamorphic ocean crust of the SMT. **(a)** SEM-BSE image showing the distributions of DCM (red arrows) in the zeolite from sample JL119-G02. **(b)** Combined SEM-BSE, shown in panel **a**, and EDS images showing the distribution of carbon in red. **(c)** SEM-EDS mappings (correspond to panel **a**), showing the distribution of carbon in red and iron in green. **(d)** SEM-BSE image showing the distributions of DCM in the zeolite from sample JL120-G02. **(e)** Combined SEM-BSE and EDS images generated from the green box in panel **d**, showing the distribution of carbon in red. **(f)** SEM-EDS map (corresponds to panel **e**), showing the distribution of carbon in red and iron in green. **(g-m)** Enlarged SEM-BSE images of various DCMs in zeolite from sample JL121-G04, showing that they are characterised by compacted patchy organic matter. Scale bars are 200 µm for panel a, 40 µm for panel d, 10 µm for panels g-m.

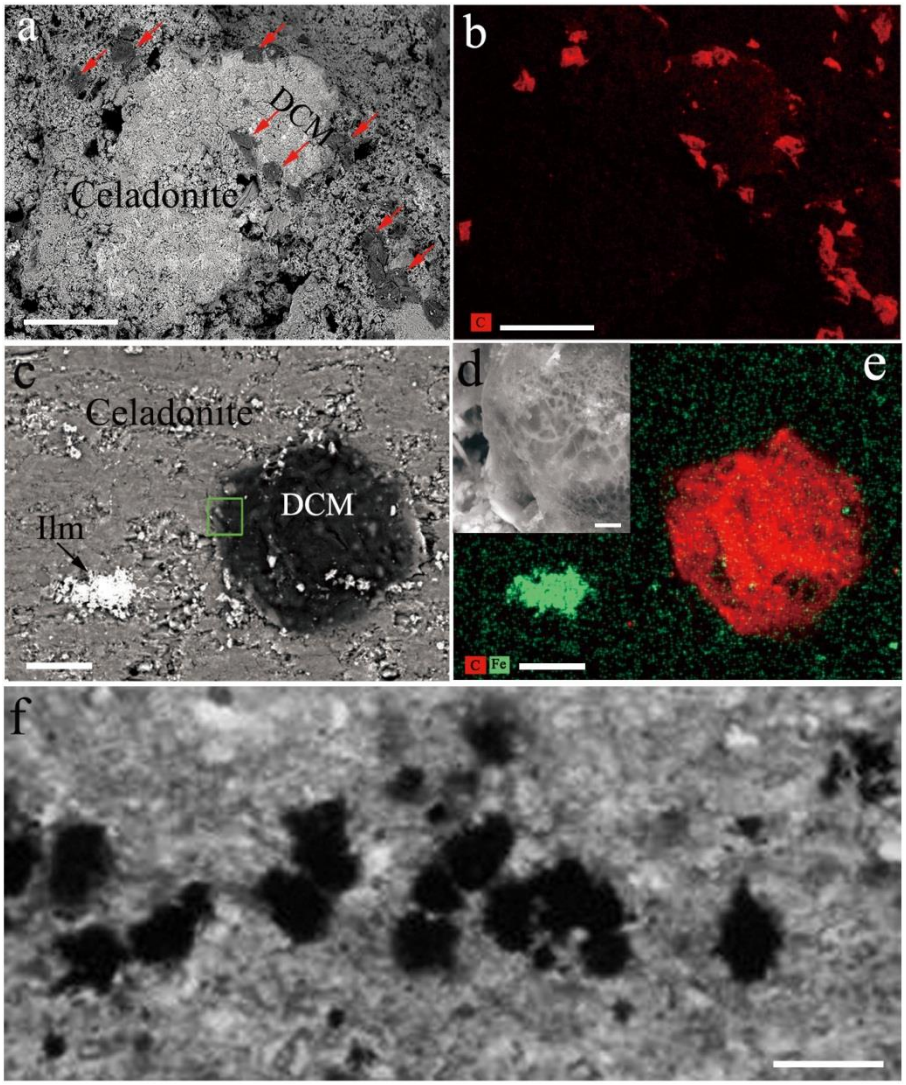

Figure S-4 Representative disordered carbonaceous matter (DCM) embedded in celadonite from the metamorphic ocean crust of the SMT (sample JL122-G02). **(a)** SEM-BSE image showing the distributions of DCM (red arrows) in celadonite. **(b)** SEM-EDS map (corresponds to panel **a**), showing the distribution of carbon in red. **(c)** SEM-BSE image of DCM in celadonite (Ilm: ilmenite). **(d)** Enlarged SEM-BSE microphotograph generated from the green box in panel **c**, showing the presence of net-like, loosely or condensed-gel structures within DCM. **(e)** SEM-EDS map (corresponds to panel **c**), showing the distribution of carbon in red and iron in green. **(f)** Transmitted white light photomicrograph of DCMs in celadonite. Scale bars are 100 µm for panels a, b, f, 10 µm for panels c, e, 1 µm for panel d.

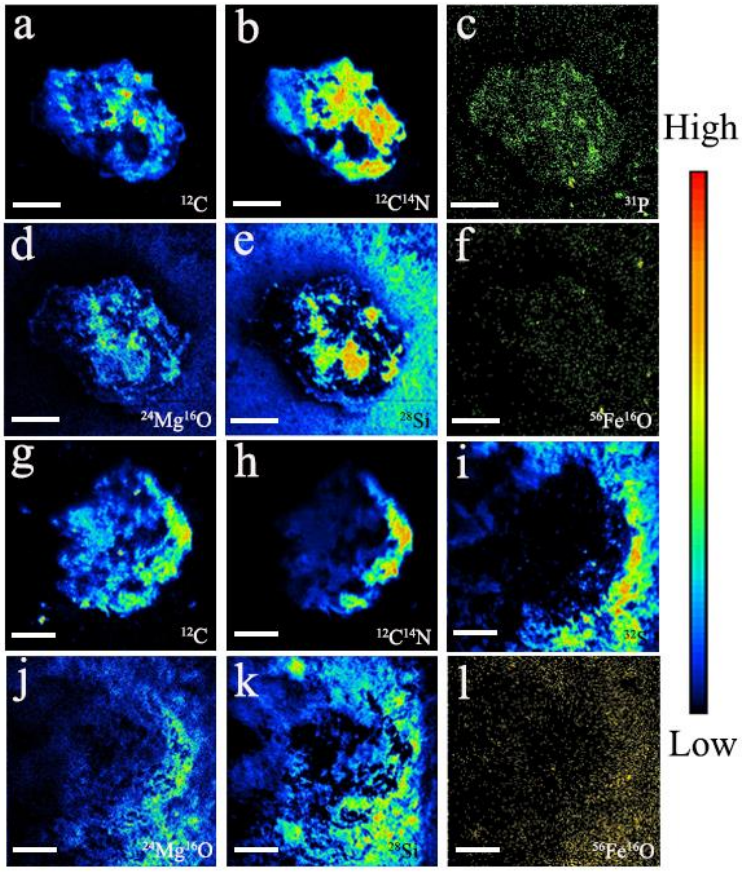

Figure S-5 NanoSIMS element maps of carbonaceous matters in celadonite from sample JL122-G01. **(a-f)** Element images of ^{12}C, $^{12}C^{14}N$, ^{31}P, $^{24}Mg^{16}O$, ^{28}Si, and $^{56}Fe^{16}O$ were generated from a loose, carbonaceous structure with oval morphology. **(g-l)** Element images of ^{12}C, $^{12}C^{14}N$, ^{32}S, $^{24}Mg^{16}O$, ^{28}Si, and $^{56}Fe^{16}O$ were generated from a loose, carbonaceous structure with rounded morphology. Note that the carbonaceous matters are chiefly composed of carbon (C), nitrogen (N) and phosphorus (P) whereas the matrix contains magnesium (Mg), iron (Fe) and silicon (Si). Ion intensity variations are shown by the calibration bar. Scale bars are 10 µm for all panels.

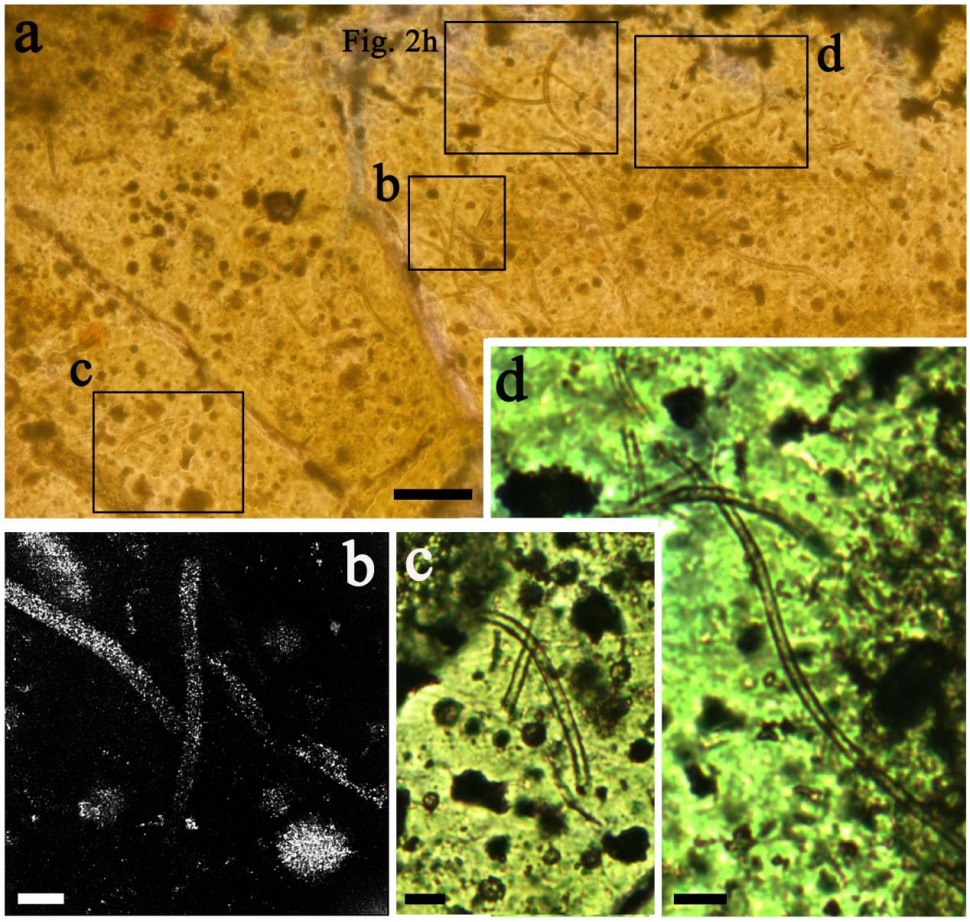

Figure S-6 Filamentous microfossils preserved in the celadonite from the metamorphic ocean crust of the south slope of SMT (sample JL122-G01). **(a)** Transmitted white light image showing the distributions of filamentous microfossils within the celadonite from polished thin section. **(b)** Two-dimensional CLSM image viewed in the plane of the thin section, rotated to an oblique view in Figure 2j. **(c-d)** Enlarged views of microfossils in panel a, showing that they are usually tubular, non-septate, unbranched filaments. The scale bar is 40 µm for panel a, 5 µm for panels b, 10 µm for panels c-d.

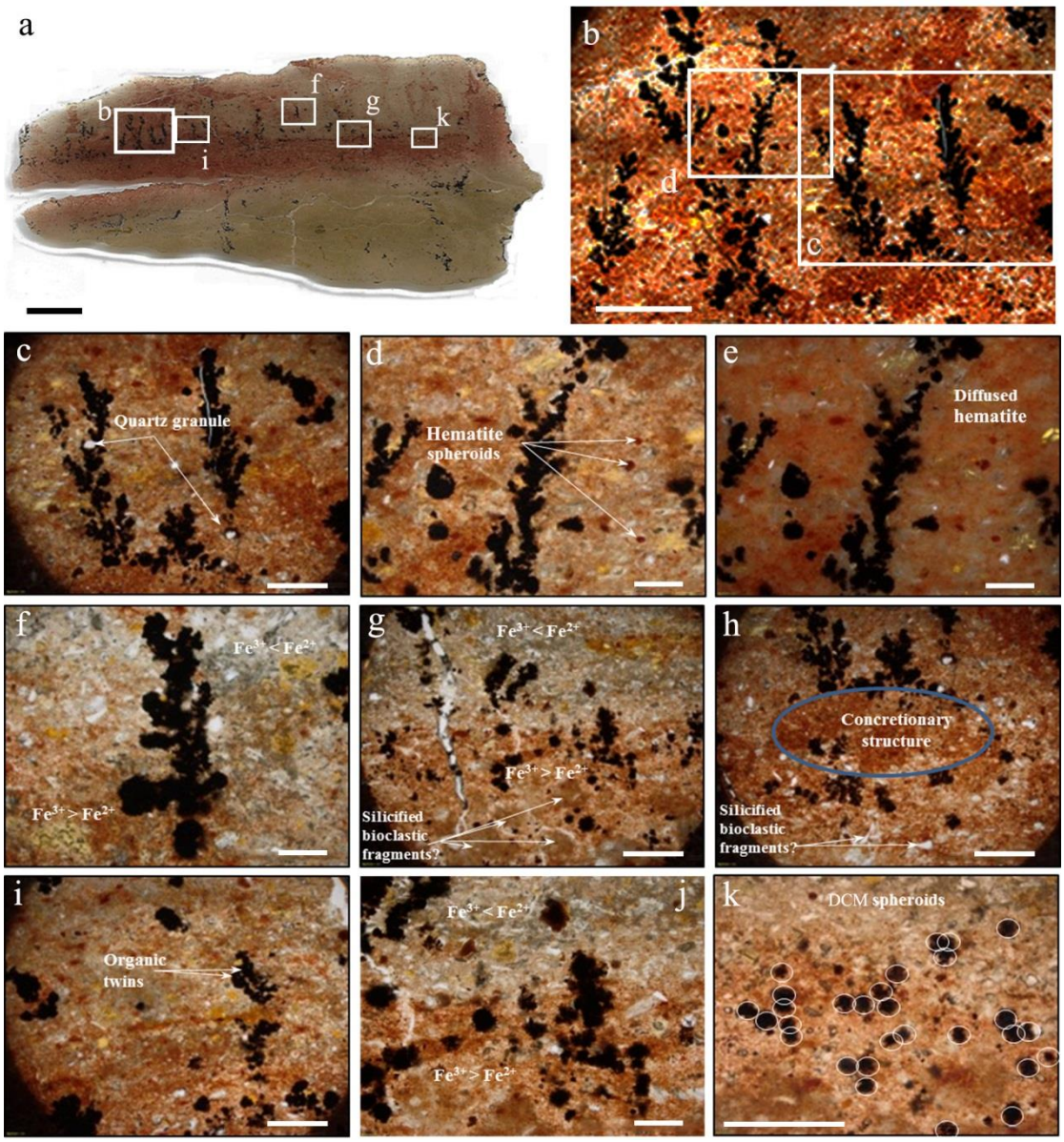

Figure S-7 *Frutexites*-like structures in celadonite from the metamorphic ocean crust of the SMT (sample JL122-G02). **(a)** The thin section showing the fields of b, f, g, i and k (white box). **(b-k)** Transmitted white light photomicrograph of *Frutexites*-like structures associated with disordered carbonaceous matter (DCM) in celadonite. Notably, the *Frutexites*-like structures occur in parts of the green rocks that are more orange to red, qualitatively with higher levels of ferric iron, which suggests that they were involved in Fe oxidation (Heim *et al.,* 2017). The scale bar is 5 mm for panel a, 1 mm for panel b, 500 µm for panels c, g-i, 200 µm for panels d-f, j-k.

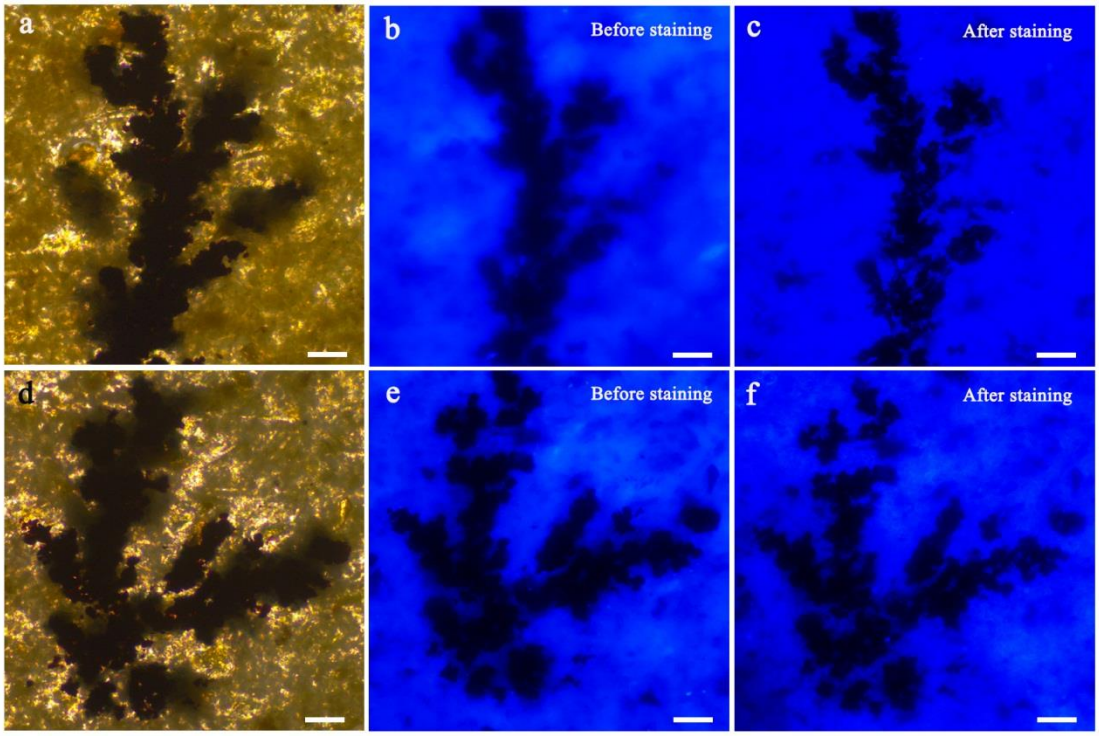

Figure S-8 Photomicrographs of typical *Frutexites*-like structures in the sample JL120-G03. **(a, d)** Transmitted white light photomicrograph of *Frutexites*-like structures. **(b, c)** Same area as **(a)** viewed with an epifluorescence microscopy before and after staining with DAPI, respectively. **(e, f)** Same area as **(d)** viewed with an epifluorescence microscopy before and after staining with DAPI, respectively. Note that no DNA was detected by DAPI in the samples, showing that DNA has been degraded and these structures may result from past growth of microorganisms. Scale bars are 50 µm for all panels.

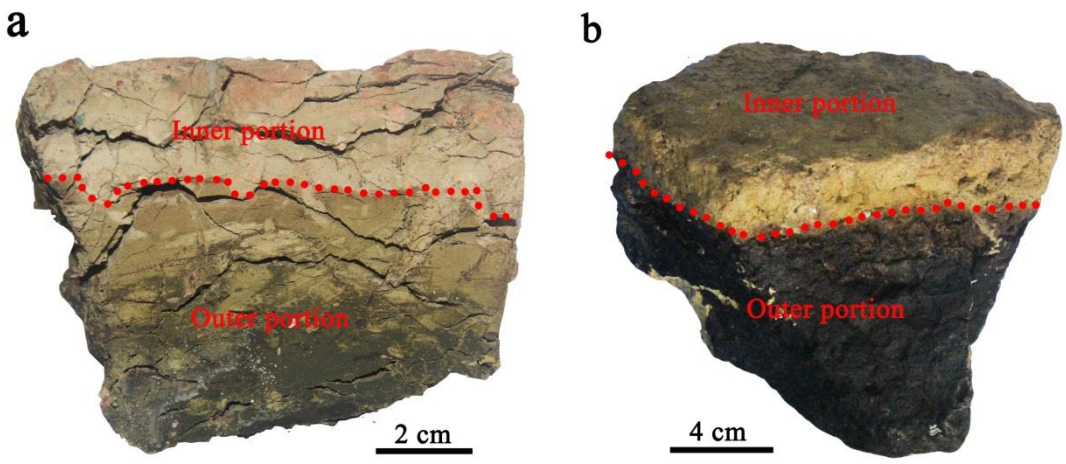

Figure S-9 The sampling sites for the inner and outer portions of metamorphic rocks selected for the lipid analysis. **(a)** The sample JL122-G02. **(b)** The sample JL121-G04.

Supplementary Video

Video S-1 Tubular filaments revealing the existence of a "hollow" lumina.

Video S-1 is available for download from the online version of this article at https://www.geochemicalperspectivesletters.org/article2017.

Supplementary Information References

Alt, J.C., Muehlenbachs, K., Honnorez, J. (1986) An oxygen isotopic profile through the upper kilometer of the oceanic crust, DSDP Hole 504B. *Earth and Planetary Science Letters* 80, 217-229.

Fang, J., Findlay, R.H. (1996) The use of a classic lipid extraction method for simultaneous recovery of organic pollutants and microbial lipids from sediments. *Journal of Microbiological Methods 27*, 63-71.

Fang, J., Lyon, D.Y., Wiesner, M.R., Dong, J., Alvarez, P.J.J. (2007) Effect of a Fullerene Water Suspension on Bacterial Phospholipids and Membrane Phase Behavior. *Environmental Science and Technology* 41, 2636-2642.

Fisk, M. R., Popa, R., Mason, O.U., Storrie-Lombardi, M.C., Vicenzi, E.P. (2006) *Astrobiology* 6, 48-68.

Guo, Z., Peng, X., Czaja, A.D., Chen, S., Ta, K. (2018) Cellular taphonomy of well-preserved Gaoyuzhuang microfossils: A window into the preservation of ancient cyanobacteria. *Precambrian Research* 304, 88-98.

Hall, A. (1993) Application of the indophenol blue method to the determination of ammonium in silicate rocks and minerals. *Applied Geochemistry* 8, 101-105.

Hopmans, E.C. et al. (2004) A novel proxy for terrestrial organic matter in sediments based on branched and isoprenoid tetraether lipids. *Earth and Planetary Science Letters* 224, 107-116.

Papineau, D., She, Z., Dodd, M.S. (2017) Chemically-oscillating reactions during the diagenetic oxidation of organic matter and in the formation of granules in late Palaeoproterozoic chert from Lake Superior. *Chemical Geology* 470, 33-54.

Peng, X., Guo, Z., House, C.H., Chen, S., Ta, K. (2016) SIMS and NanoSIMS analyses of well-preserved microfossils imply oxygen-producing photosynthesis in the Mesoproterozoic anoxic ocean. *Chemical Geology* 441, 24-34.

Schouten, S., Hopmans, E.C., Sinninghe Damsté, J.S. (2013) The organic geochemistry of glycerol dialkyl glycerol tetraether lipids: a review. *Organic Geochemistry* 54, 19-61.

Sturt, H.F., Summons, R.E., Smith, K., Elvert, M., Hinrichs, K.U. (2004) Intact polar membrane lipids in prokaryotes and sediments deciphered by high performance liquid chromatography/electrospray ionisation multistage mass spectrometry‐new biomarkers for biogeochemistry and microbial ecology. *Rapid Communications in Mass Spectrometry* 18, 617-628.

Weijers, J.W.H., Schefu, E., Kim, J.H., Sinninghe Damsté, J.S., Schouten, S. (2014) Constraints on the sources of branched tetraether membrane lipids in distal marine sediments. *Organic Geochemistry* 72, 14-22.

Winter, J.D. (2010) Principles of Igneous and Metamorphic Petrology. Second Edition, Prentice Hall, New Jersey, 541–548.

Xie, W., Zhang, C.L., Ma, C.L. (2015) Temporal variation in community structure and lipid composition of Thaumarchaeota from subtropical soil: Insight into proposing a new soil pH proxy. *Organic Geochemistry* 83-84, 54-64.

Xu, H., Chen, T., Konishi, H. (2010) HRTEM investigation of trilling todorokite and nano-phase Mn-oxides in manganese dendrites. *American Mineralogist* 95, 556-562.